Available online at www.sciencedirect.com

ScienceDirect

Advances in Space Research 56 (2015) 218–228

ADVANCES IN SPACE RESEARCH (a COSPAR publication)

www.elsevier.com/locate/asr

Improving space debris detection in GEO ring using image deconvolution

Jorge Núñez [a,b,*], Anna Núñez [c], Francisco Javier Montojo [d], Marta Condominas [e]

[a] Departament d'Astronomia i Meteorologia and Institut de Ciències del Cosmos (ICC), Universitat de Barcelona (UB/IEEC), Av. Diagonal 647, 08028 Barcelona, Spain

[b] Observatori Fabra, Barcelona, Spain

[c] Facultat de Medicina, Universitat de Barcelona, Spain

[d] Real Instituto y Observatorio de la Armada, San Fernando 11110, Cádiz, Spain

[e] Department de Política Econòmica i Estructura Econòmica Mundial, Universitat de Barcelona, Av. Diagonal 690, 08028 Barcelona, Spain

Received 7 December 2014; received in revised form 22 February 2015; accepted 6 April 2015
Available online 11 April 2015

Abstract

In this paper we present a method based on image deconvolution to improve the detection of space debris, mainly in the geostationary ring. Among the deconvolution methods we chose the iterative Richardson–Lucy (R–L), as the method that achieves better goals with a reasonable amount of computation. For this work, we used two sets of real 4096 × 4096 pixel test images obtained with the Telescope Fabra-ROA at Montsec (TFRM). Using the first set of data, we establish the optimal number of iterations in 7, and applying the R–L method with 7 iterations to the images, we show that the astrometric accuracy does not vary significantly while the limiting magnitude of the deconvolved images increases significantly compared to the original ones. The increase is in average about 1.0 magnitude, which means that objects up to 2.5 times fainter can be detected after deconvolution. The application of the method to the second set of test images, which includes several faint objects, shows that, after deconvolution, up to four previously undetected faint objects are detected in a single frame. Finally, we carried out a study of some economic aspects of applying the deconvolution method, showing that an important economic impact can be envisaged.

Keywords: Space debris; Image processing; Image deconvolution; Maximum likelihood method

1. Introduction

The space debris problem is nowadays considered a growing threat to space operations, both manned and automatic (IAA position paper, 1993, 2001; Schildknecht, 2007). Even some experts propose a scenario in which the volume of space debris would reach a limit such that the collision rate be enough high to generate a cascade of new space debris. This situation, which is known as the Kessler effect (Kessler, 1991), could cause the inability to use the space at least in certain orbits, in particular, the Low Earth Orbit (LEO). In the case of the Geostationary Orbit (GEO) and the ring around it, the problem of space debris is very important because it is a privileged orbit with an orbital period equal to the Earth's rotation, densely populated and the home of the main satellites devoted to communications, TV, Meteorology, Remote sensing, etc.

The present technology does not allow the removal of space debris, hence the best option is cataloging as many space debris as possible and the precise knowledge of the orbits of these dangerous objects (Montojo et al., 2011a).

* Corresponding author at: Departament d'Astronomia i Meteorologia and Institut de Ciències del Cosmos (ICC), Universitat de Barcelona (UB/IEEC), Av. Diagonal 647, 08028 Barcelona, Spain. Tel.: +34 93 402 1129.
E-mail address: jorge@am.ub.es (J. Núñez).

http://dx.doi.org/10.1016/j.asr.2015.04.006
0273-1177/

The radar observation is useful for LEO objects (up to 2000 km) but it is not efficient for objects in Medium Earth Orbit (MEO) and in GEO (at 36,000 km) because the efficiency of the radar decreases with the fourth power of the distance. Therefore, observations using telescopes of large optical Field of View (FOV) is the best choice for the detection and orbit computation of objects in the GEO orbit. Thus, it is very important to maximize the number of space debris that can be detected in an image, particularly the faint ones. To detect faint objects, the standard method is to make images of large exposure time, but, in the case of orbital objects, such way is not possible due to the large motion of the objects with respect to the reference stars. Yanagisawa et al. (2005) propose a technique based on stacking many frames but, the CCD images must be shifted to fit the movement of the object, so various shift values of the moving object must be investigated to guess the motion of the unknown object. This is a handicap in the case of non-GEO space debris that present appreciable motion in hour angle and declination.

Another way is to take relatively short exposures and to apply image processing technics to enhance the faint objects.

In this work we developed the application of image processing to increase the limiting magnitude of the optical observations and, consequently, increase the number of faint space debris that can be detected and measured in an image. However, the classical approaches to enhance the faint details in an image, as the contrast increment, histogram equalization or high pass filters are little effective and increment notably the noise in the image. Thus, we apply the image deconvolution technique as the best way to enhance the faint objects in the image, allowing for the detection and astrometric positioning of them. To do this, in Section 2 we present the basics of the method to improve the detection of faint objects, the image deconvolution theory and the used algorithms. In Section 3 we described the telescope and data utilized in the study. Section 4 is devoted to present the specific software used, the Point Spread Function model, the computing requirements and the obtained results. The results show the ideal number of iterations to perform, the preservation of the astrometric accuracy in the process, the improvement in limiting magnitude and presents some practical examples showing the increment in the number of faint objects detected. Section 5 is devoted to present some aspects of the economic impact of the proposed method and Section 6 the conclusions of the work.

2. Improving faint space debris detection

2.1. Basics of the method

As stated above, the best way to detect and catalog space debris in MEO and GEO orbits is using optical images taken with large Field of View (FOV) telescopes. Satellites and space debris appear in optical images as objects that move very fast regarding the stars that appear in the same image. If we take a frame tracking the sky, a moving object is shown in the image as a trail, loosing easily the faint objects. If we take a frame tracking a moving object (for example stopping the telescope to observe objects in GEO orbit), the moving objects should appear as point sources. However, the ideal point-like image of the object appears convolved with several mathematical functions due to the optics of the telescope, the optical aberrations, the atmosphere, the characteristics of the detector, etc. In a typical frame this convolution makes point-like objects appear as pixelized extended light spots, which is the result of the convolution of the point source with the Point Spread Function (PSF), plus sampling. This convolution with the PSF does not affect the integral Signal to Noise Ratio (SNR), but decreases the SNR of the peak and, therefore, the chances to be detected. Furthermore, the images of other objects, not exactly in the same orbit, appear as short trails and the images of the stars as long trails.

The basic idea of the method is to use image deconvolution techniques to improve the SNR of the objects present in the image increasing, as a result, the optical detection of faint space debris. Hence, computer programs that automatically seek space debris can detect more objects. For example, if one of these programs has a detection threshold of SNR = 2.0, i.e. it is able to find all objects that have a signal 2 times higher than the background noise of the image, the program will not detect objects having a SNR smaller than 2.0 and all these objects will be lost. If the processing of the image allows to increase the SNR, it is possible that some objects that were below the threshold to be now over it and, therefore, can be detected. A direct consequence of this improvement is what is known as increasing the limiting magnitude. The magnitude of an object is measured in logarithmic scale of its brightness in a way that the higher the magnitude the fainter is the object. Therefore, the limiting magnitude indicates the faintest detectable object.

On the other hand, it is known that the usual software for image manipulation used to increase the image quality as, for example, a High Pass Filter to increase the contrast, present as a counterpoint an increased image noise. This fact can make some noise image points that were below the detection threshold to pass above the detection limit, causing an unacceptable number of false detections. Thus, in this study, we will not consider such software and will center the study on the image deconvolution methods as the methods to increase the SNR but controlling the noise amplification.

2.2. Image deconvolution

As stated above, in an image of the sky taken to observe either stars or orbital objects (satellites, space debris, etc.) the object of interest appears convolved with the PSF. Mathematically, the process can be described as an

imaging equation which is a relationship between the light distribution of the source $\boldsymbol{a}$ (the ideal image) and $\boldsymbol{p}$, the observed image by the sensor. After discretizing the problem, the imaging equation can be written as: $\boldsymbol{F} * \boldsymbol{a} + \boldsymbol{b} + \boldsymbol{n} = \boldsymbol{p}$, where $\boldsymbol{a}$ and $\boldsymbol{p}$ are the unknown and data vectors respectively, and $\boldsymbol{n}$ and $\boldsymbol{b}$ are vectors representing the readout noise and the background in both object and data spaces and $\boldsymbol{F}$ is a sparse matrix representing the PSF. In the case of the stars appearing in an image taken in stare mode (tracking the sky), the PSF can be understood as the actual image of a point-like star (mostly represented by a Gaussian-like pattern). In the case of orbital objects, the PSF is understood as the actual image recorded on the frame by the moving satellite or space debris. In this case, the shape of the PSF will depend of the observing strategy. If the observation is tracking the object (for example, as stated above, stopping the telescope to detect GEO objects), the PSF corresponding to the object is the image of a point-like source. Note that $\boldsymbol{a}$, $\boldsymbol{p}$, $\boldsymbol{n}$ and $\boldsymbol{b}$ represent, in general, two-dimensional images but since they are discretized, they can be represented as vectors.

Image deconvolution consists in obtaining the best approximation of the ideal image $\boldsymbol{a}$ from the inversion of the imaging equation. However, it is well known this problem is an ill-posed noisy inverse one. Thus, the imaging equation cannot be correctly solved by linear methods such as matrix inversion or the direct Fourier inversion since these methods magnify the noise providing unacceptable results.

For a long time, image deconvolution was considered a luxury in optical astronomy, remote sensing or satellite tracking. However, since the discovery in 1990 of a severe problem of spherical aberration in the mirror of the Hubble Space Telescope (HST) a substantial amount of work has been done in this field directed towards optical and near-IR astronomy (with applications in other fields), covering different types of data noise and proposing dozens of algorithms.

2.3. Deconvolution algorithms used

Several publications describe the dozens of algorithms developed for image deconvolution. We direct the reader to the published excellent proceedings as White and Allen (1990), Hanisch and White (1994); special issues: Núñez (1995) and reviews: Molina et al. (2001), Starck et al. (2002). In these works the reader can find, among many others, algorithms based in Maximum Likelihood, Maximum Entropy and the Bayesian paradigm. Specific astrometric application to assess the recovery of faint stars was directed in Girard et al. (1995), Prades and Núñez (1997), Fors (2006), Núñez (2013). An application to the satellites and Space debris case was developed in Fors et al. (2010).

In this work we used two different algorithms: (a) The Richardson–Lucy (R–L) algorithm (Richardson, 1972; Lucy, 1974), a classical algorithm widely used in Astronomy, in the version for Poisson data with Gaussian readout noise as the CCD cameras (Núñez and Llacer, 1993, 1998) and (b) The Adaptive Wavelet-decomposition-based Maximum Likelihood (AWMLE) method (Otazu, 2001; Starck et al., 2002), a more sophisticated algorithm that shows a better noise amplification control and asymptotically convergence but at expenses of much higher computing time.

Since the results of both algorithms do not differ significantly in this case (increase of the SNR and astrometric accuracy) and the R–L algorithm is much faster (about 20 times faster), we will present only results for the later. Furthermore, the R–L algorithm for CCD cameras is available in free astronomical software such as the Image Reduction and Analysis Facility (IRAF) and in widely used astronomical commercial packages as MaxIm DL. Hence, the R–L algorithm for Poisson data with Gaussian readout noise is one of the most easily accessible software for image deconvolution, allowing that other researchers working in Space debris could easily use the method.

In summary (see the given references for details), the R–L algorithm for CCD images is an iterative Maximum Likelihood algorithm, but truncated well before reaching the maximum. At each iteration, the provisional result is compared with a noise-filtered version of the data and the provisional image is updated. This operation involves, at each iteration, four Fast Fourier Transforms (FFT) of the whole image.

3. Data used

3.1. The Telescope Fabra-ROA Montsec (TFRM)

In this paper we use images taken with the Fabra-ROA Telescope Montsec (TFRM). The telescope (Fors et al., 2013) is located at the Serra del Montsec, 1570 m high. The telescope is the transformation for CCD observation of a Baker-Nunn telescope of 50 cm aperture made by NASA, which was designed to track artificial satellites. The TFRM, with its CCD camera of 4096×4096 pixels, is ideal for observing space debris thanks to its large Field of View ($4.4° \times 4.4°$) and its focal ratio (focal length/aperture telescope) of 0.96, i.e. extremely bright, which allows shorter exposures and for operating in fully robotic mode (Montojo et al., 2011b).

Each TFRM image is of 4096×4096 pixels in FITS format (Wells et al., 1981) and contains several thousands of images of stars. Given its huge Field of View, the telescope can register, near the GEO ring, up to some tens of satellites and space debris in a single image. Furthermore, the TFRM can observe satellites and space debris in any GEO, MEO and LEO orbit thanks to its tracking system able to adapt the telescope motion to the speed of the object.

3.2. Images of the Hispasat constellation zone

For this study we chose two groups of images of the TFRM. The first group consists of 42 images taken on 25/05/2011 in the GEO zone of the sky where the constellation of Hispasat satellites is placed (Hispasat, 1992–2012). This group has been used mainly for studies on astrometric accuracy and gain in limiting magnitude. The second group consists of a series of six images, taken on 28/10/2012, in which there are both easily detectable bright objects and faint objects that are not automatically detected in the original images. This second set of images were taken in an area of the sky of lower altitude and, therefore, more difficult to observe, is appropriate to demonstrate the validity of the new method of deconvolution to detect faint objects.

4. Results

4.1. Software used

For the R–L deconvolution algorithm, in this work we used the implementation of MaxIm DL. This election is because the differences in the results between this implementation and our own implementation (Núñez and Llacer, 1993) or the IRAF implementation are minimal and the MaxIm DL implementation is easier to use for the common user not familiarized with astronomical software.

Once the images are deconvolved, the analysis of the resulting images, in comparison with the original ones, was carried out using the Apex-II package (Devyatkin et al., 2010), TFRM-tools and PinPoint Astrometric Engine. Apex-II is a complete package developed at Pulkovo Observatory that carries out the astrometric reduction, the morphological identification of the orbital objects and the establishment of the tracks of the individual objects (Kouprianov, 2008). This software is used and widely validated by the International Scientific Optical Network (ISON), which is one of largest net of telescopes specializing in observation of space objects (Molotov et al., 2014; Kouprianov, 2012). TFRM-tools is a similar software package developed by the TFRM team. For the astrometric reduction, the morphological identification of orbital objects and the establishment of the tracks, the TFRM-tools package uses, respectively, scripts based on the Dynamic-link Library (DLL) of the PinPoint Astrometric Engine; the PinPoint implementation of the SExtractor software (Bertin and Arnouts, 1996), and a series of programs for the cross-correlation of the orbital objects between the images. The PinPoint Astrometric engine is a commercial software devoted mainly to minor planets research but it can be also used for the manual astrometric reduction of images and to find individual positions of objects. PinPoint, however, is not useful for automatic detection of fast moving objects such as space debris. The visualization of original and deconvolved images was carried out using MaxIm DL and SAOImage-DS9 (see web links below; SAOImage DS9, 1990–2014).

4.2. CPU time

The computer time needed to carry out one iteration in the R–L algorithm is, basically, the time needed to perform out the 4 FFTs involved since all the other computations are vector operations that have little impact on CPU time. Although this is an intensive computation on the 4096×4096 pixel images of the TFRM, the present computers can carry out one R–L iteration in few seconds. For example, using the MaxIm DL implementation, a modest laptop computer (based in an Intel i3 processor at 2.53 GHz with 6 GB of RAM) carries out a R–L iteration of a full TFRM image in 15 s. Of course, faster multiprocessor computers can perform the computation in much less CPU time. This means that using the R–L algorithm truncated after few iterations (see below), the CPU time needed for the deconvolution process is not a limitation.

4.3. PSF model

For the PSF model, it is possible to use either a Gaussian-like pattern or, if possible, the image of a real object. In this work we used the image of a real bright but unsaturated geostationary object. Since the Field of View of the TFRM is huge, it is easy to find some of them in the image. Although in this work, we chose the object to represent the PSF manually, it is easy to find a good candidate automatically using the morphology of the objects given by the SExtractor algorithm. Alternatively, if it is not possible to find a real object in the image as PSF model, a Gaussian pattern works also reasonably well.

4.4. Iteration number

As stated above, the R–L algorithm is an iterative algorithm going towards the Maximum Likelihood solution but stopped before reaching the maximum. This is because the R–L solution is an unconstrained "classical" solution of the ill-posed integral imaging equation. The result is that the iterative R–L algorithm produces solutions that are highly unstable, with high peaks and deep valleys. Thus, it is necessary to stop the process before reaching convergence. To compute the stopping point of the algorithm, several approaches have been proposed. In the above cited reviews and proceedings, the reader can find most of them (from pure visual inspection to highly mathematical methods). Probably, the most robust method to stop the algorithm is the cross-validation tests, which compute the likelihood of the solution with respect to an alternative set of data (cross-likelihood). The stopping point is given by the maximum of the cross-likelihood against the iteration number (Núñez and Llacer, 1993). However, the cross-validation analysis is difficult to perform because

two independent but equivalent images are needed. If tracking the sky, this is possible to obtain making two consecutive images of the same exposure time, but this is not possible tracking orbital objects, as in the GEO ring, because all the stars moved between them. Also, dividing randomly the image is only an approximation in CCD cameras because the readout noise. Furthermore the cross-validation analysis is more CPU time consuming since two sets of deconvolutions have to be done.

To make the presented method easier for the user not familiarized with deconvolution software, in this work we used the much more familiar Chi-squared test. In the case of deconvolution, the Chi-squared test compares the real data (the original image) with the projection (by convolution) of the deconvolved image taking into account, in this comparison, the expected differences given by the typical noise of the light distribution in the image.

The imaging equation $\boldsymbol{F} * \boldsymbol{a} + \boldsymbol{b} + \boldsymbol{n} = \boldsymbol{p}$ can be written in components:

$$\sum_{i=1}^{N} F_{ji} a_i + b_j + n_j = p_j; \quad j = 1, \ldots, N$$

where N is the total number of pixels. In this notation, the Chi-squared is defined as

$$\chi^2 = \frac{1}{N} \sum_{j=1}^{N} \frac{\left(\sum_{i=1}^{n} F_{ji} a_i + b_j + n_j - p_j\right)^2}{p_j}$$

If we let the R–L algorithm to go to full convergence, the mathematical solution trends to make the projection of the solution $\boldsymbol{F} * \boldsymbol{a} + \boldsymbol{b} + \boldsymbol{n}$ as similar as possible to the data $\boldsymbol{p}$, making the numerator of the Chi-squared expression as little as possible ($\chi^2 \to 0$) but, as stated above, at expenses of unacceptable artifacts in the solution. However, for an Imaging Pulse Counting System (the CCD cameras approximate it) in which the arrival of photons at a pixel is Poisson distributed around the mean, the difference $\sum_{i=1}^{n} F_{ji} a_i + b_j + n_j - p_j;\ j = 1, \ldots, N$ presents a standard deviation of $\sqrt{p_j}$. Hence, in case of a perfect deconvolution, the expected value of the left summation is N and the expected value of χ^2 is 1.0.

Fig. 1 plots the Chi-squared against the number of iterations for one of the 42 test images described in Section 3.2.

As stated, for the distribution of light in images of astronomical CCD cameras, the ideal value of the Chi-squared test is 1.0, but values slightly above or below are acceptable depending on the characteristics of the image and the quality of deconvolution, so a value of about 1.3 may be perfectly valid. In Fig. 1 it is easy to see that a number of iterations of about 7 is enough to reach an acceptable value of the Chi-squared from the statistical point of view. We applied the test to several of the 42 test images obtaining very similar results. It is important to point out also that, although in theory the Chi-squared test should be performed to all images, in practice once established the optimal number of iterations for some images, this number is valid for all the images of the set.

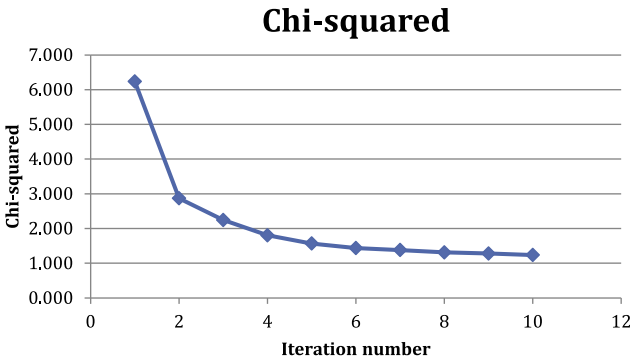

Fig. 1. Evolution of the Chi-squared against the number of iterations for a R–L deconvolution of one of the test images.

4.5. Astrometric accuracy

A critical point of this study is to verify that the deconvolution process does not affect the astrometric accuracy of the deconvolved images, as this would invalidate the method. The astrometric accuracy is measured in the standard way as the Root Mean Square (RMS) of reference stars with respect to catalog. Firstly, the plate is solved adjusting a polynomial (usually of 4th degree) of transformation between the Cartesian coordinates of the stars and the astronomical positions of the stars in the reference catalog. Then the astrometric accuracy is computed as the RMS of the differences between the computed (using the transformation polynomial) astrometric positions of the stars in the image and the cataloged positions. Of course, this is the global error of the plate and only the lower limit on the final error of an object which includes the particular error in the centroid position of the object.

The astrometric accuracy of the original images in the test set was of about 0.8 arc seconds. This is a typical value for TFRM images devoted to space debris in GEO orbit (trailed stars). As can be seen in Fig. 2, after the first two iterations, the astrometric accuracy remains constant and very close to the original given by iteration number 0.

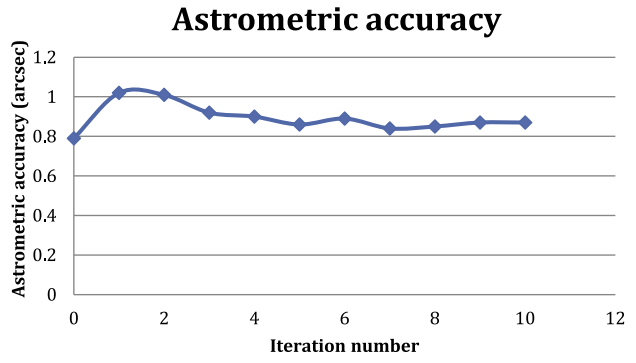

Fig. 2. Evolution of the astrometric accuracy against the number of iterations for the test images.

Again, the other images in the test set present the same behavior. This result shows that the deconvolution method has no negative impact on the global accuracy that remains constant during the process and very close to the original one. This result shows that the deconvolved images have the same astrometric accuracy as the original ones.

4.6. Improving the limiting magnitude

The main goals of this work is to achieve, using deconvolution, that the limiting magnitude of the deconvolved images be higher than that of the original ones since, as mentioned above, the limiting magnitude indicates the magnitude of the faintest object that can be detected. As can be seen in Fig. 3, the limiting magnitude is between 0.5 and 1.5 magnitudes higher respect to the original image (iteration 0) regardless of the number of iterations fixed by the stopping point criterion. This means that now it is possible to detect weaker space debris in the deconvolved images. Since the magnitude's scale is logarithmic, this increment means that it is possible to detect objects between 1.5 and 4 times weaker.

It is important to point out that, apparently, attending to the gain in limiting magnitude, the algorithms should be stopped at iteration 1 or 2, but, at that number of iterations, the image is not well developed and the faint real objects are still not detectable. This is due to the fact that the computation of the limiting magnitude is carried out using the McLean (2008) relation in which several parameters, as the S/N ratio or the number of pixels over which a point source is distributed, have no much sense before reaching an acceptable level of deconvolution. Hence, we must establish the stopping point first (using the stopping point criterion) and then check if, at that point, the limiting magnitude has increased or not. The aim of Fig. 3 is to show that the limiting magnitude is higher in the deconvolved image than in the original one regardless of the stopping point fixed by the stopping criterion.

Given the results of Chi-square test, astrometric accuracy and limiting magnitude, we appreciate that a number of iterations between 6 and 8 gives correct results for the three indicators. Hence, in this work we adopted the value of 7 as the number of iterations for the stopping point of the algorithm.

Once established the ideal number of iterations in 7, it is important to show that the limiting magnitude improves in all the images and not just in some of them or in a specific area of the sky. So, we deconvolved all the 42 images of the test set. Although all images correspond to the same constellation of satellites, as taken at different times, these correspond to independent areas of the sky. In Fig. 4 it is shown that the limiting magnitude increases in all cases, which shows that the method works for different images from different parts of the sky. On average the increment in limiting magnitude for the 42 images is about 1.0 magnitudes (from 16.4 to 17.4). Taking into account that the difference of magnitudes between two objects is given by the expression $\Delta m = 2.5\log_{10}(I_2/I_1)$ where I_2 and I_1 are the respective intensities of the objects, an increment of magnitude of $\Delta m = 1.0$ means that it is possible to detect objects about 2.5 times fainter.

Note that image number 22 presents a different behavior respect the others. This is because it has, by chance, the saturated trail of a bright LEO satellite crossing part of the image. Hence, probably, the computation of the limiting magnitude in the original image was wrong. We could disregard this image, but we preferred to keep it in order to not bias the sample.

Of course, different nights will present different conditions as seeing size, sky background level, etc. which will change day by day. In order to show that the gain in limiting magnitude was not thanks to a particular set of images, we performed several tests using images of different nights obtaining increments in limiting magnitude between 0.8 and 1.4 approximately. Hence, we set the expected limiting magnitude gain in about 1.0 mag. But, obviously, the gain will depend of the conditions of the particular night.

4.7. Examples of detection of new faint objects

Once the effectiveness of deconvolution to increase the limiting magnitude has been shown, it is worth to show

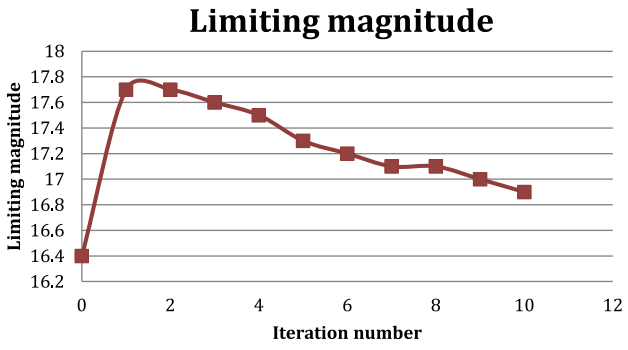

Fig. 3. Evolution of the value of the limiting magnitude depending on the number of iterations images Hispasat.

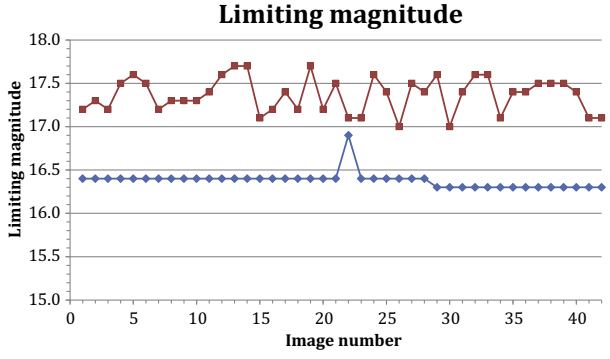

Fig. 4. Limiting magnitude for the 42 test images before (blue) and after deconvolution (red). (For interpretation of the references to color in this figure legend, the reader is referred to the web version of this article.)

some examples of detection of faint objects that were not detected in the original images. For this purpose we used the second set of images described in Section 3.2 in which appear some bright objects detected easily in the original images but also other faint objects not detected. We established a S/N ratio of 2.5 as detection criterion and carried out the deconvolution of all the images of the set using the method of Richardson–Lucy with 7 iterations. Fig. 5 shows the profile of an object not detected in the original image and the profile of the same object in the deconvolved image. Both images are plotted at the same scale. As can be seen in the figure, the gain in SNR is large, which may allow now for detection. Also, the Full Width at Hal Maximum (FWHM) of the profile decreases, as expected in a deconvolution process.

Fig. 6 (left) shows how the PinPoint is able to find, in the original image, the astrometric position of two bright objects (blue crosses) but not the third, which corresponds to a faint object similar to the one displayed in Fig. 5. However, as can be seen in Fig. 6 (right), using the same parameters, thanks to the increased SNR, the object is easily detected in the deconvolved image (yellow cross). Fig. 7 shows the full-field image of one of the images of the series. The red circles are objects detected in the original image (7 objects) and the green circles are new detected objects (4 objects) after deconvolution.

Fig. 8 shows in detail the bottom right of the Fig. 7 where it is possible to see more clearly the detection of the new geostationary object (green circle) shown in Fig. 6. In the image it is also possible to see the trace left by a faster satellite.

Table 1 summarizes the results about the total number of objects candidate (by morphology), detected true objects, limiting magnitude, accuracy and FWHM before and after deconvolution for the group of images used in the test.

Regarding the FWHM, it is important to point out that the FWHM is difficult to measure in images obtained tracking orbital objects (as the images of the GEO ring of the example) in which the stars appear as long trails. We estimated the FWHM of the images using the round images of the GEO satellites present in the images and, also, the profiles perpendicular to the trails left by the images of some non-saturated stars. In Table 1, the FWHM pass from about 3.2 pixels in the original images to about 2.3 pixels after deconvolution, which is an important improvement. Note that this numbers are coherent with a deconvolution process and with the original

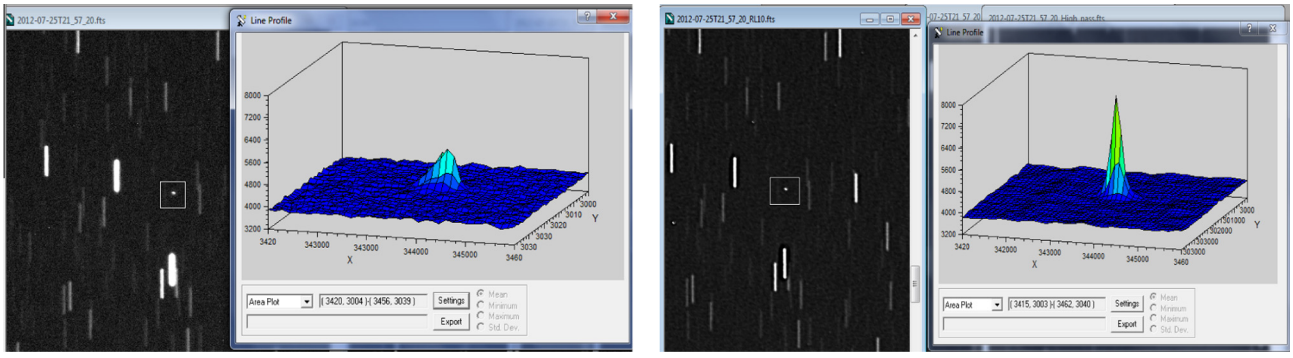

Fig. 5. Profile of an orbital object in the original image (left) and in the deconvolved image (right) plotted at the same scale (in the images *N* is at left, so the trailed image of the stars appear up to down).

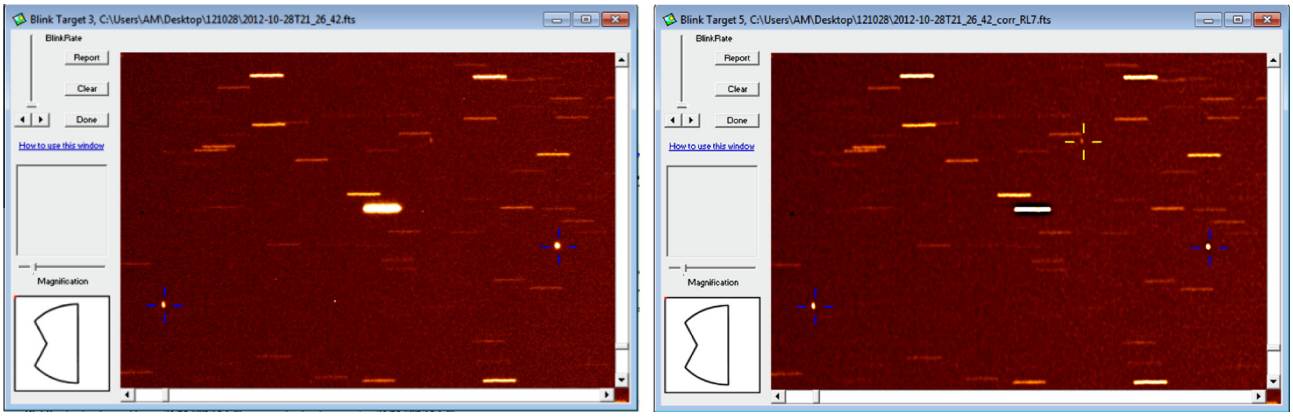

Fig. 6. Detection of orbital objects in one of the original images (left) and in the deconvolved one (right) with the location of an additional object (yellow cross). (For interpretation of the references to color in this figure legend, the reader is referred to the web version of this article.)

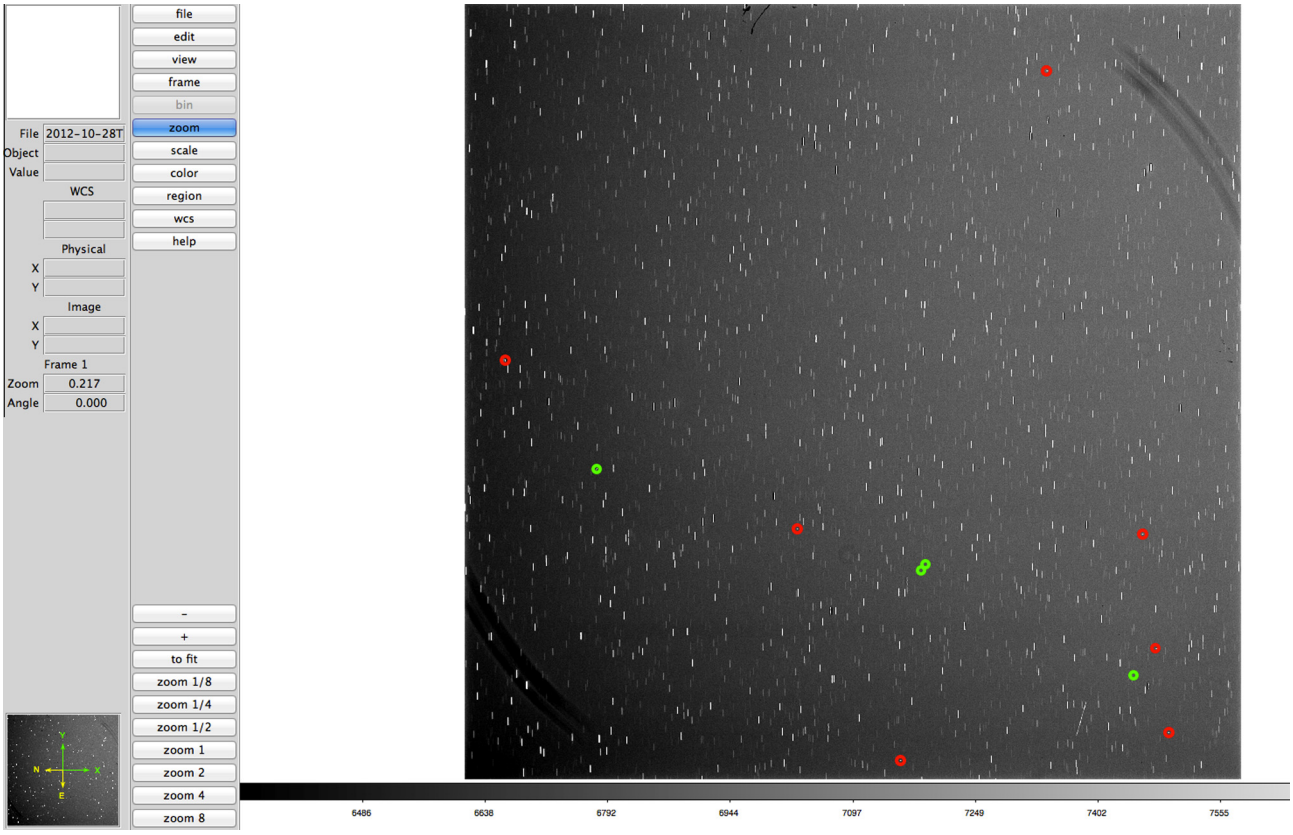

Fig. 7. Detection of four new objects (green circles) in one deconvolved image of the series. Red circles indicate the seven objects previously detected in the original. (For interpretation of the references to color in this figure legend, the reader is referred to the web version of this article.)

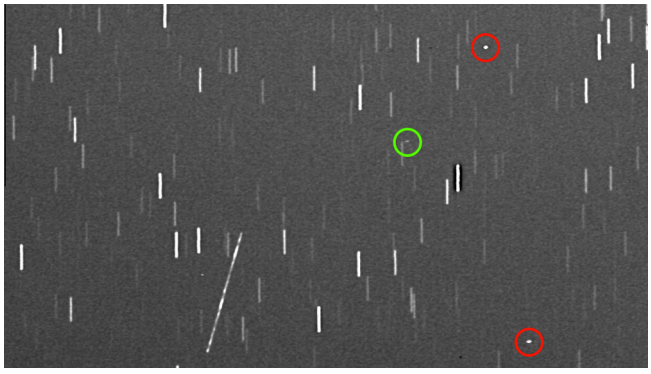

Fig. 8. Detail (bottom right) of Fig. 7 showing the location of the new space object (green circle) of Fig. 6. The trace left by a faster satellite is also shown (*N* is at left, so the trailed image of the stars appear up to down). (For interpretation of the references to color in this figure legend, the reader is referred to the web version of this article.)

Baker-Nunn optical system, designed to include the 80% of the light in a circle of 20 microns of diameter (2.2 pixels in the TFRM). The addition of three new optical elements (meniscus, filter and field-flattener) during the TFRM refurbishment along with some defocusing justifies the differences.

However, during the deconvolution process, always appear artifacts in form of amplified bright noise peaks, cosmic rays, etc. that mimic the morphology of stars or, in our case, the GEO objects. With the size of the FWHM of the original and deconvolved images, real objects may become morphologically indistinguishable from the artifacts. Hence, the number of false detections increases notably and could become a real problem. Obviously, the impact in the performance depends a lot on the cross-correlation analysis program and the speed of the computer used. In Table 1 it is depicted the number of objects identified by morphology as candidates to be orbital objects for the original and deconvolved images.

As expected, the number of candidates and, therefore, the number of false detections increases from few (up to 14) in the original images to tens (up to 99) in the deconvolved ones. This is a notable increment, but the number of candidates is still manageable for the cross-correlation analysis. To do the cross-correlation, we used a routine of TFRM-tools consisting in a C program running in a Mac OSX-10 with a 2.2 GHz Intel Core i7 and 16 GB RAM. For the 6 original images of the example, the program reaches the solution almost instantaneously and for the set of deconvolved images again in less than a second. Of course there is an important increment in terms of combinations of candidates to check (in terms of factor), but not very high in terms of absolute CPU time since it represents much less than the time to carry out one of the deconvolutions. Hence, in this example, the false detections rate has little impact in the total computation time. Also, faster

Table 1
Number of candidates, detected true objects, limiting magnitude, astrometric accuracy and FWHM in the original and deconvolved images.

Image	Original image					Deconvolved image (RL 7 iterations)				
	Total candidates	Detected objects	Limiting magnitude	Accuracy (″)	FWHM (pixels)	Total candidates	Detected objects and increment	Limiting magnitude and increment	Accuracy (″)	FWHM (pixels)
2012-10-28-1	13	7	15.6	0.71	3.0	36	11 (57%)	16.8 (1.2)	0.79	2.1
2012-10-28-2	9	7	15.5	0.73	3.6	99	9 (29%)	17.0 (1.5)	0.79	2.8
2012-10-28-3	14	8	15.6	0.72	3.2	68	9 (13%)	17.1 (1.5)	0.85	2.1
2012-10-28-4	9	7	15.5	0.68	3.1	30	8 (14%)	16.8 (1.3)	0.81	2.2
2012-10-28-5	10	6	15.5	0.73	3.1	42	7 (17%)	16.9 (1.4)	0.76	2.2
2012-10-28-6	11	7	15.5	0.73	3.0	30	8 (14%)	16.8 (1.3)	0.82	2.2

computers in the coming years will help to decrease the CPU time.

Of course, the main results of this example is regarding to the number of true objects detected, the limiting magnitude and the astrometric accuracy. In Table 1 it is seen that the number of detected objects is always higher, between 13% and 57%, in the deconvolved images than in the original. The same happens in the case of the limiting magnitude, which increases between 1.2 and 1.5 magnitudes, while the accuracy does not vary significantly. Note the difference in the number of detections in the first image. It is worth to say that the object highlighted in Figs. 6 and 8 was not detected in any of the original images but it was detected in all of the deconvolved ones. Regarding the number of tracks detected, in the series of original images a total of 6 tracks were detected while in the series of deconvolved images, the total number of tracks was 7. This is an important increment that could have been much higher since in the first image of the series of deconvolved images, other three faint objects were detected but, probably because of object's rotation, they were too faint in the other images of the series to be recovered even after deconvolution. If the effect of the rotation had been a little smaller, the method could have recovered more faint objects.

The results show the usefulness of the method of image deconvolution to improve the limiting magnitude and, as a consequence, the number of space debris that can be detected in optical images. These results together with the fact that the astrometric accuracy remains constant during the process, shows, also, the correct choice of the Richardson–Lucy method and the number of iterations carried out.

5. Possible economic impact

Independently of the scientific aspects of the proposed method, another interesting point to consider is the possible economic impact of applying the deconvolution to the optical images for space debris. As stated in Section 4.6, we should consider that a gain of about 1.0 magnitude allows detecting objects 2.5 times fainter. This means that the effect of the deconvolution is equivalent to make 2.5 longer exposures or to have a telescope with 2.5 times the collecting surface (diameter 1.6 times larger).

Using as example the TFRM telescope, assuming a yearly maintenance cost of about $250,000 (including part of the salaries of technicians and astronomers) and an effective useful observing time of 50% (assuming the other 50% lost by bad weather and breakdowns), we can derive a cost of about $1400 per useful night. Taking into account that the telescope usually carries out exposures of 10 s and uses another 10 s for reading the image and repositioning (in a cycle of about 20 s), we could reduce the exposure time to 4 s, so a cycle of 14 s could be obtained. Such reduction of the cycle represents a 30% or, equivalently, the possibility to do in one night the work of 1.4 nights, increasing the "production" in a 40%. From the economic point of view, the possibility to do in one year the work of 1.4 years represents savings of $0.4 * 250{,}000 = \$100{,}000$ in maintenance costs. It is important to point out that shorter exposures lead to shorter star trails, which may make difficult to distinguish star trails from orbital objects by morphology. However, we consider that the star trails left in a 4 s exposure is enough, at least for TFRM images, to allow the morphology filter to work properly.

Another way to see to the economic benefits of the deconvolution is to estimate the cost of a telescope able to reach the same limiting magnitude in the original images. As stated above, the effect of deconvolution is to reach the same limiting magnitude of a telescope 1.6 times larger in diameter. Assuming that the price of a telescope is proportional to the square of the diameter, such price would be 2.5 times higher and the maintenance cost would be also higher by about the same factor.

Other source of economic impact but difficult to quantify is the fact that this technique could improve the general knowledge of the space debris population. Such improvement would help to better avoid the risk of collision and close encounters between space debris and active satellites, with the economic impact that avoiding such collisions would have.

Of course, the deconvolution process is not free in terms of computer time. However, as stated in Section 4.2, the CPU time needed to perform a single iteration by the R–L method using a single processor computer is of few seconds. This means CPU time of the order of one minute for a full deconvolution. Also, as stated above, the deconvolution process adds false candidate detections increasing

the CPU time needed for the cross-correlation of the orbital objects between the images to find the tracks. However, if the number of iterations is limited (7 in this study) this effect has little impact in the total computation time. Given that a powerful multiprocessor computer, as the 64 kernel TFRM main computer, can do the full 7–10 iteration process in few seconds, costs less than $10,000 and can last at least three years, the needed extra computing resources has little impact from the economic point of view.

6. Conclusions

In this work we have developed a method based on deconvolution of optical images to improve the detection of space debris, mainly in the geostationary ring. Deconvolution is an advanced technique that requires intensive computation and knowledge of the Point Spread Function (PSF). It is a process that attempts to retrieve the image to its original state, removing effects such as optical aberrations, atmospheric turbulence or the noise characteristic of the image. Among the deconvolution methods we have chosen the Richardson–Lucy method (R–L), which is an iterative Maximum Likelihood as the method that achieves better goals with a reasonable amount of computation.

The study was performed using two sets of images obtained with the Fabra-ROA Telescope Montsec, totaling 48 images of 4096×4096 pixels. The sets of data correspond to the Hispasat constellation area and another area with bright and faint objects. The R–L deconvolution of test images shows that the astrometric accuracy does not vary significantly with the number of iterations. This is very important to ensure that the image quality is preserved during the process. On the other hand, the limiting magnitude of the deconvolved images increases significantly compared to the original ones. The increase is between 0.5 and 1.5 magnitudes, depending on the image and the number of iterations. This is the key of this study because it shows that the Signal to Noise Ratio increases, facilitating the detection of space debris that were previously too weak to be detected.

The study of the Chi-square test on the images indicated that the ideal number of iterations is 7 for this kind of images. The application of the R–L method with 7 iterations to the 42 test images of the first set, represents an increment in limiting magnitude of 1.0 magnitudes in average, which means that it can be detected objects up to 2.5 times weaker. The application of the method to the set of test images with previously undetected faint objects shows, depending on the image, up to four (57%) new detections as well as an increase in limiting magnitude between 1.2 and 1.5 magnitudes that means to detect objects between 3 and 4 times weaker.

Finally, we carried out a study of some economic aspects of applying the deconvolution method, showing that an important economic impact can be envisaged.

These results leads to the general conclusion that the deconvolution process can help to notably increase in the number of space debris detectable in the optical images, which can contribute to improving the knowledge and cataloging of these orbital dangerous objects.

7. Web links

<http://www.cyanogen.com/maxim_main.php>: MaxImDL® Diffraction Limited, Cyanogen Imaging Prods. Inc.

http://pinpoint.dc3.com>: PinPoint Astrometric Engine®, DC-3 Dreams®.

<http://ds9.si.edu/site/Whats_New.html>: SAOImage DS9.

Acknowledgments

This effort was supported by Departament d'Economia i Coneixement of the Catalonian Government (several grants). The authors acknowledge support of the TFRM team for preparing and carrying out the optical observations used in this paper.

References

Bertin, E., Arnouts, S., 1996. SExtractor: Software for source extraction. Astron. Astrophys. Supp. 117, 393–404.

Devyatkin, A.V., Gorshanov, D.L., Kouprianov, V.V., Verestchagina, I.A., 2010. Apex I and Apex II software packages for the reduction of astronomical CCD observations. Sol. Syst. Res. 44 (1), 68–80.

Fors, O., 2006. New observational techniques and analysis tools for wide field CCD surveys and high resolution astrometry (Ph.D. thesis). University of Barcelona. <http://www.tesisenxarxa.net/TESIS_UB/AVAILABLE/TDX-0330106-125745//OFA_TESI.PDF>.

Fors, O., Núñez, J., Otazu, X., Prades, A., Cardinal, R.D., 2010. Improving the ability of image sensors to detect faint stars and moving objects using image deconvolution techniques. Sensors 10 (3), 1743–1752.

Fors, O., Núñez, J., Muiños, J.L., Montojo, F.J., Baena, R., Boloix, J., López-Morcillo, R., Merino, M.T., Downey, E.D., Mazur, M.J., 2013. Telescope Fabra ROA Montsec: a new robotic wide-field Baker-Nunn facility. Publ. Astron. Soc. Pac. 927, 522–528.

Girard, T.M., Li, Y., van Altena, W.F., Núñez, J., Prades, A., 1995. Astrometry with reconstructed HST planetary camera (WF/PC 1) images. Int. J. Imaging Syst. Technol. 6 (4), 395–400, Special Issue on Image Reconstruction and Restoration in Astronomy.

Hanisch, R.J., White, R.L. (Eds.), 1994. The Restoration of HST Images and Spectra II. STScI, Baltimore, U.S.A..

Hispasat Spanish communication satellites, 1992–2012. Instituto Nacional de Técnica Aeroespacial (INTA).

IAA Position Paper on Orbital Debris, 1993. Acta Astronaut., vol. 31, pp. 169–191.

IAA Position Paper on Orbital Debris updated version of IAA position paper on orbital debris, 2001. ESA SP-473, vol. 2, pp. 841–849.

Kessler, D.J., 1991. Collisional cascading: the limits of population growth in low earth orbit. Adv. Space Res. 11, 63–66.

Kouprianov, V., 2008. Distinguishing features of CCD astrometry of faint GEO objects. Adv. Space Res. 41 (7), 1029–1038.

Kouprianov, V., 2012. Apex II + FORTE: data acquisition software for space surveillance. In: 39th COSPAR Scientific Assembly. Held 14–22 July 2012, in Mysore, India. Abstract PPP.2-3-12, p. 974.

Lucy, L., 1974. An iterative technique for the rectification of observed distributions. Astron. J. 79, 745.

McLean, I., 2008. Electronic Imaging in Astronomy: Detectors and Instrumentation, second ed. Springer, New York and Heidelberg.

Molina, R., Núñez, J., Cortijo, F., Mateos, J., 2001. Image restoration in astronomy. A Bayesian perspective. IEEE Signal Process. Mag. 18 (2), 11–29.

Molotov, I., Agapov, V., Zalles, R., Voropaev, V., Zolotov, V., Kokina, T., Montojo, F.J., Namkhai, T., 2014. Current status of the ISON optical network. In: 40th COSPAR Scientific Assembly. Held 2–10 August 2014, in Moscow, Russia, Abstract PEDAS.1-3-14.

Montojo, F.J., López-Moratalla, T., Abad, C., 2011a. Astrometric positioning and orbit determination of geostationary satellites. Adv. Space Res. 47, 1043–1053.

Montojo, F.J., Fors, O., Muiños, J.L., López-Morcillo, R., Baena, R., Boloix, J., López-Moratalla, T., Merino, M., 2011b. The Fabra-ROA telescope at Montsec (TFRM): a fully robotic wide-field telescope for space surveillance and tracking. In: Proceedings of the European Space Surveillance Conf., Madrid, 7–9 June 2011.

Núñez, J., 1995. Image reconstruction and restoration in astronomy. Int. J. Imaging Syst. Technol. 6 (4), Special Issue on Image Reconstruction and Restoration in Astronomy.

Núñez, J., 2013. Image deconvolution. In: Astrometry for Astrophysics. Methods, Models and Applications. Cambridge University Press, pp. 265–276.

Núñez, J., Llacer, J., 1993. A general Bayesian image reconstruction algorithm with entropy prior. Preliminary application to HST data. Publ. Astron. Soc. Pac. 105, 1192–1208.

Núñez, J., Llacer, J., 1998. Bayesian image reconstruction with space-variant noise suppression. Astron. Astrophys. Suppl. Ser. 131, 167–180.

Otazu, X., 2001. Algunes aplicacions de les Wavelets al procés de dades en astronomía i teledetecció (Ph.D. thesis). University of Barcelona. <http://www.tesisenxarxa.net/TESIS_UB/AVAILABLE/TDX-0325103-090215//tesi_xavier_otazu2.pdf>.

Prades, A., Núñez, J., 1997. Improving astrometric measurements using image reconstruction. In "Visual double stars. formation, dynamics and evolutionary tracks". ASSL 223, 15–25.

Richardson, W., 1972. Bayesian-based iterative method of image restoration. J. Opt. Soc. Am. Ser. A. 62 (3), 55–59.

SAOImage DS9, 1990–2014. Smithsonian Astrophysical Observatory. Cambridge, MA, 02138.

Schildknecht, T., 2007. Optical surveys for space debris. Astron. Astrophys. Rev. 14 (1), 41–111.

Starck, J.L., Pantin, E., Murtagh, F., 2002. Deconvolution in astronomy: a review. Publ. Astron. Soc. Pac. 114, 1051–1069.

Wells, D.C., Greisen, E.W., Harten, R.H., 1981. FITS: a flexible image transport system. Astron. Astrophys. Suppl. Ser 44, 363–370.

White, R.L., Allen, R.J. (Eds.), 1990. The Restoration of HST Images and Spectra. STScI, Baltimore, U.S.A..

Yanagisawa, T., Nakajima, A., Kadota, K., Kurosaki, H., Nakamura, T., Yoshida, F., Dermawan, B., Sato, Y., 2005. Automatic detection algorithm for small moving objects. Publ. Astron. Soc. Japan 57, 399–408.